

Modeling and fabrication of chip-based superconducting traps for levitation of micrometer-sized superconducting particles

Martí Gutierrez Latorre,¹ Joachim Hofer,² Matthias Rudolph,¹ and Witlef Wiczorek^{1,*}

¹*Department of Microtechnology and Nanoscience (MC2),
Chalmers University of Technology, Kemivägen 9, SE-412 96 Gothenburg, Sweden*

²*Vienna Center for Quantum Science and Technology (VCQ), Faculty of Physics,
University of Vienna, Boltzmanngasse 5, Vienna, A-1090, Austria*

We describe the finite-element modeling and fabrication of chip-based superconducting traps for levitating micrometer-sized superconducting particles. Such experiments promise to lead to a new generation of macroscopic quantum experiments and of force and acceleration sensors. An accurate modeling of the utilized trap architectures is crucial for predicting parameters of the traps, such as trap stability, frequency and levitation height, in realistic situations accounting for the finite extent of the involved superconducting objects. To this end, we apply a modeling method that is applicable to arbitrary superconducting structures in the Meissner state. It is based on Maxwell-London equations in the static regime using the A-V formulation. The modeling allows us to simulate superconducting objects with arbitrary geometry subject to arbitrary magnetic field distributions and captures finite volume effects like magnetic field expulsion. We use this modeling to simulate two chip-based trap architectures: an anti-Helmholtz coil-type trap and a planar double-loop trap. We calculate important parameters of the superconducting traps for the cases of levitating micrometer-sized particles of either spherical, cylindrical or ring shape. We compare our modeling results to analytical test cases for idealized geometries. We also model detection of the motion of the levitated particle by measurement of flux-changes induced in a nearby pick-up loop. We demonstrate the fabrication of the analyzed chip-based traps and particles using thin Nb films. Our modeling is generic and has applications beyond the one considered, such as designing superconducting magnetic shields or for calculating filling factors in superconducting resonators.

I. INTRODUCTION

Superconducting magnetic levitation^{1,2} is a fascinating phenomenon and its applications range from demonstration experiments³ to precise measurements of gravity using the superconducting gravimeter⁴. Recently, theoretical proposals suggest the use of superconducting magnetic levitation as a means to enable new experiments in the field of quantum optics^{5,6}. Specifically, micrometer-sized superconducting or magnetic objects levitated by magnetic fields are proposed to lead to a new generation of quantum experiments that enable spatial superposition states of levitated objects^{5–8} or ultra-high sensitivities for measurement of forces or accelerations^{7,9,10}, with recent experiments along these lines^{11–16}.

Superconducting magnetic levitation experiments require superconducting traps that generate magnetic field distributions that are capable of levitating superconducting particles. As a superconducting particle is a perfect diamagnet, the traps require a local magnetic field minimum accompanied by a field gradient for achieving stable levitation¹⁷. For the cases we consider, the levitated particles and the associated traps have dimensions on the order of micrometers. Such micrometer-sized traps can be fabricated using standard techniques developed for superconducting thin films, as we exemplify using thin films of Nb¹⁸. Superconducting chip-based trap structures have already been developed in the context of atom

optics for trapping atomic clouds on top of superconducting chips^{19–22}. However, in contrast to trapped atomic clouds, a levitated particle has a finite extent and, thus, requires accounting for its volume and the finite magnetic field penetration in the levitated object such that trap properties can be accurately predicted. Analytical formulas exist for idealized geometries, such as for a diamagnetic sphere in a quadrupole field⁵ or in a field of four parallel wires⁸, for a superconducting sphere in a quadrupole field²³, for a diamagnetic ring in a quadrupole field²⁴ or can be derived for symmetric geometries and diamagnetic objects using the image method²⁵. However, in the general case when considering realistic trap geometries of reduced symmetry, trap wires of finite extent or arbitrary shapes of the levitated particle, analytical formulas do not exist and one has to resort to modeling using finite-element methods (FEM).

In this work, we use FEM-based simulations to calculate trap parameters, such as trap stability, frequency and levitation height, for realistic superconducting chip-based trap geometries capable of levitating superconducting particles of different shape and size. We further demonstrate the fabrication of superconducting trap architectures using thin Nb films, the fabrication of ring or cylinder-shaped Nb particles and the selection of spherical Pb particles from commercially available Pb powder.

Our FEM simulations are based on implementing Maxwell-London equations in the static regime using the A-V formulation under the assumption that all superconducting structures are in the Meissner state^{26–29}. We apply this modeling to analyze in detail two realistic trap

* witlef.wiczorek@chalmers.se

structures, micrometer-sized multilayer anti-Helmholtz coil-like (AHC) and single layer double-loop traps. We compare the modeling results to more ideal situations of increased symmetry, where analytical results can be obtained^{23,25,30}. We note that the presented FEM modeling can also be used for simulating larger trap structures and particles, which are interesting in the context of acceleration sensing^{9,13}. We consider levitation of different particle shapes, such as spheres, cylinders and rings, and, crucially, incorporate flux quantization in case of levitation of a ring. Our models are generic and can be applied to other settings involving superconductors in the Meissner state.

Our work is structured as follows. In Sec. II we summarize the underlying simulation model and in Sec. III state the principles for realizing stable magnetic levitation. We describe the fabrication of the two considered trap architectures and of different particle shapes in Sec. IV. We turn to the simulation of the traps in Sec. V and discuss the results in the light of achieving stable levitation. In Sec. VI we analyze measurement of the center-of-mass motion of a particle levitated in a superconducting trap and calculate the expected signal detected in a pick-up loop. We conclude our work in Sec. VII. The appendix contains details on the modeling method (Appendix A), the validation of our modeling against test cases (Appendix B), dependence of the results on the FEM mesh (Appendix C), additional simulation results (Appendix D) and the relation between the Maxwell stress tensor, forces and fields (Appendix E).

II. MODELING

The FEM simulations we use, are based on a simplification of the Ginzburg-Landau equations for the superconducting state in the limiting case of small external magnetic field \mathbf{B} . Ginzburg-Landau theory predicts for a superconductor under a magnetic field, that its supercurrent \mathbf{J}_s is given by³¹:

$$\mathbf{J}_s = i \frac{e\hbar}{2m} (\Psi^* \nabla \Psi - \Psi \nabla \Psi^*) - \frac{2e^2}{m} \mathbf{A} |\Psi|^2, \quad (1)$$

where e and m are the charge and mass of the electron, respectively, \hbar is the reduced Planck constant, \mathbf{A} is the magnetic vector potential, Ψ is the wave-function that describes the cooper pair density in the superconductor, and $|\Psi|^2$ is the cooper pair density. The cooper pair density gets smaller once an external magnetic field \mathbf{B} is applied, and equals zero when \mathbf{B} is larger than the critical field \mathbf{B}_c . Conversely, in the absence of a magnetic field, $|\Psi|^2$ is maximum and constant. For small magnetic fields $|\Psi|^2$ decreases only slightly, making $\nabla \Psi$ and $\nabla \Psi^*$ negligible. Thus, the equation for the supercurrent reduces to the London model³¹:

$$\mathbf{J}_s = -\frac{1}{\mu_0 \lambda_L^2} \mathbf{A}, \quad (2)$$

where $\lambda_L = \sqrt{\frac{m}{\mu_0 |\Psi|^2 e^2}}$ is the London penetration depth and μ_0 the magnetic permeability of vacuum. By implementing this equation in FEM software as an external contribution to the current density in the superconductor domains, one can model domains as type I superconductors in the Meissner state. The model solves the Maxwell-London equations using \mathbf{A} -V formulation^{26–29}. That is, the field equations are solved using the magnetic vector potential \mathbf{A} and the voltage V as the dependent variables, for details see Appendix A. In our case, the field equations are solved in the quasi-static regime, so time derivatives of the equations describing the system are not involved. We would like to point out that describing dynamic systems is, however, possible as shown in Ref.³². We note that, if \mathbf{B} is larger than the first critical field, \mathbf{B}_{c1} , magnetic flux vortices will start nucleating in the superconductor and the gradient terms in Eq. (1) cannot be neglected. Thus \mathbf{B}_{c1} puts a bound on the maximal trap strength that is achievable in our modeling, along with the critical current density \mathbf{J}_c in the coil material. Future work could extend our modeling by, e.g., using the critical state model³³ applicable to hard type-II superconductors.

Another feature of superconductivity is fluxoid quantization, which should be accounted for to accurately describe superconducting objects with holes. In our case, this concerns the levitation of ring-like particles. Fluxoid quantization can be derived by integrating Eq. (1) over a closed loop in the superconductor, which contains a hole with magnetic flux Φ_{hole} . This results in³¹:

$$\frac{m}{2e^2 |\Psi|^2} \oint_C \mathbf{J}_s \cdot d\mathbf{l} = \frac{\hbar}{2e} \oint_C \nabla \theta \cdot d\mathbf{l} - \oint_C \mathbf{A} \cdot d\mathbf{l} = \Phi_0 n - \Phi_{\text{hole}}, \quad (3)$$

where θ is the phase of the wave function, n an integer, and $\Phi_0 = h/2e$ is the magnetic flux quantum. Eq. (3) tells us that the supercurrent will preserve the magnetic flux threading the hole of the superconductor as the multiple of Φ_0 closest to Φ_{hole} .

Since our model does not account for the contribution of the wave function's gradient, fluxoid quantization cannot emerge from the implementation of Eq. (2). We simplify our modeling by considering only flux quantization in the following and, thus, neglect the flux in the ring's interior material caused by the finite penetration depth of the external magnetic field. This approximation is reasonable for $\Lambda/R \ll 1$ (we have $\Lambda/R < 0.05$), where $\Lambda = \lambda_L^2/d$ is the two dimensional effective penetration depth, R is the size of the superconducting object and d the superconducting film thickness³⁴. We implement flux quantization ad hoc by defining the area of the hole in the superconductor over which Eq. (3) is integrated and impose an additional contribution to the current density of the superconductor such that the constraint

$$\Phi_0 n - \Phi_{\text{hole}} = 0 \quad (4)$$

is fulfilled within the defined area. In this way, a superconductor with trapped flux in a hole can be modeled.

To perform the modeling we use COMSOL Multiphysics³⁵. Equations (1) and (4) are implemented in the magnetic formulation module in the quasi-static regime. We verified our modeling against test cases, where analytical results exist and find perfect agreement, see Appendix B.

III. PRINCIPLES OF MAGNETIC LEVITATION

The goal of the chip-based traps is to stably levitate a superconducting particle in a point \mathbf{r}_{lev} in free space above the surface of the chip. To this end, a local energy minimum in the potential energy landscape $U(\mathbf{r})$ of the superconducting particle is required, with $U(\mathbf{r})$ given by¹⁷:

$$U(\mathbf{r}) = -\frac{1}{2} \int_V \mathbf{M}(\mathbf{r}) \cdot \mathbf{B}(\mathbf{r}) dV + mgz, \quad (5)$$

where \mathbf{M} is the magnetization and m the mass of the particle, g is the gravitational acceleration and z is the height above the chip surface. The integration goes over the volume of the levitated particle. For illustration, let us assume the superconducting particle to be a perfect diamagnetic point particle with magnetic moment $\mathbf{m} = V\mathbf{M} = -V\mathbf{B}/\mu_0$. Then, the force acting on the particle is¹⁷:

$$\mathbf{F}(\mathbf{r}) = -\nabla U(\mathbf{r}) = -\frac{V}{\mu_0} \mathbf{B} \cdot \nabla \mathbf{B} - \rho V g \mathbf{e}_z \quad (6)$$

and we see that levitation is achieved when $\mathbf{F}(\mathbf{r}_{\text{lev}}) = 0$, that is, when $\mathbf{B} \cdot \nabla \mathbf{B} = -\mu_0 g \rho \mathbf{e}_z$ at \mathbf{r}_{lev} . In reality, we cannot make the above approximation and we need to evaluate Eq. (5) for realistic geometries, see Appendix E for details how this is implemented in FEM.

While balance of forces is a necessary condition, it is not sufficient. Additionally, the local energy minimum at $\mathbf{r} = (x, y, z)^T = \mathbf{r}_{\text{lev}} = (x_{\text{lev}}, y_{\text{lev}}, z_{\text{lev}})^T$ must fulfill¹⁷ $\partial^2 U(\mathbf{r})/\partial x^2 > 0$, $\partial^2 U(\mathbf{r})/\partial y^2 > 0$ and $\partial^2 U(\mathbf{r})/\partial z^2 > 0$ in order to achieve stable levitation, so that the particle experiences a restoring force in the trap.

For the traps under consideration, our simulations show that for small particle displacements (on the order of 100's of nanometers) the force acting on the particle can be approximated linearly, with $\mathbf{F}(\mathbf{r}) = (F_x, F_y, F_z)^T = (k_x x, k_y y, k_z z)^T$ and k_i being the spring constant of the trap along direction i . Then, the frequency with which the particle oscillates is

$$\omega_i^2 = \frac{1}{m} \frac{\partial F_i}{\partial x_i} = \frac{1}{m} k_i, \quad (7)$$

where $(x_1, x_2, x_3)^T \equiv (x, y, z)^T$.

Assuming that thermal energy is driving the particle's motion, the root mean square oscillation amplitude $x_{\text{rms},i}$ in a given direction i for the particle being in thermal equilibrium with the environment at temperature T is:

$$x_{\text{rms},i} = \sqrt{\frac{k_B T}{m \omega_i^2}}, \quad (8)$$

where k_B is Boltzmann's constant. Typically, this amplitude is much smaller than the particle or the trap region, e.g., for a realistic situation that we consider, we assume a $1 \mu\text{m}$ Nb particle at a temperature of $T = 4 \text{ K}$ in a trap with $\omega_z = 2\pi \cdot 1 \text{ kHz}$ and obtain $x_{\text{rms},z} = 25 \text{ nm}$.

IV. FABRICATION OF CHIP-BASED SUPERCONDUCTING TRAPS AND PARTICLES

We consider superconducting trap architectures that can be used to stably levitate superconducting objects of spherical, cylinder or ring shape. We focus specifically on a chip-based micrometer-sized anti-Helmholtz coil trap and a planar double-loop trap. We put particular focus on the capability to microfabricate these traps and particles in order to guarantee reproducible parameters and scalable device architectures.

A. Fabrication of anti-Helmholtz coil-type trap

The AHC-type trap is formed by two coils arranged in an anti-Helmholtz-like configuration. Such a trap configuration is chosen as it yields a large gradient in the trap center resulting in appreciable trap frequencies as we will show in Sec. V A. Fig. 1(a) shows a schematic and Fig. 1(b,c) scanning electron microscope (SEM) images of a microfabricated trap with $3 \mu\text{m}$ inner coil radius and $1 \mu\text{m}$ vertical coil separation. Note, that we deviated from the ideal coil separation of $3 \mu\text{m}$ for this particular example due to limitations in growing thick layers of the Si spacing layer. Alternatively, one can pattern a hole of $2 \mu\text{m}$ diameter to approach an ideal AHC-trap, as modeled in Sec. V A. The layers Nb/Si/Nb are $300/1000/300 \text{ nm}$ thick, respectively, and were sequentially deposited on a Si substrate by sputtering. Each of the layers was separately structured via electron beam lithography (EBL) or optical lithography and subsequently etched using inductively coupled plasma-reactive ion etching (ICP-RIE)³⁶. The lowermost Nb coil is fabricated first and covered by Si. The Si layer is deposited and subsequently etched via RIE to expose the contact pads of the lowermost Nb coil. Then, the upper Nb layer is deposited and structured. An electrical connection between the lower and upper Nb layers is facilitated by the Nb material sputtered on the sidewalls of the openings in the Si layer. Finally, a hole is etched from the top of the Si layer down into the Si substrate. The volume contained in the hole is the trap region.

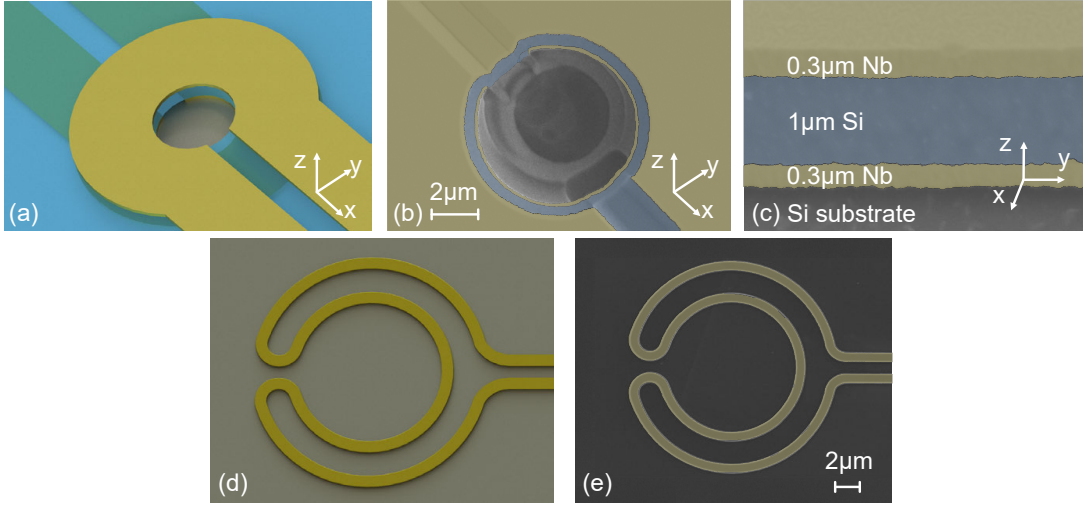


Figure 1. Schematic drawings of (a) an anti-Helmholtz coil (AHC) trap and (d) a double-loop trap. Scanning electron microscope (SEM) images showing (b) the top view of the AHC trap center where the particle will levitate. Panel (c) shows the cross section of the three-layer AHC trap device, going from the Silicon (Si) substrate through the bottom Niobium (Nb) coil, the insulating Si spacer layer, and the top Nb coil. Panel (e) shows the SEM image of a microfabricated double-loop trap. The yellowish region marks a 300 nm thick and 1 μm wide Nb wire on a Si substrate.

B. Fabrication of double-loop trap

An alternative trap arrangement consists of two concentric and co-planar coils with counter-propagating currents that generate a local energy minimum above the plane of the coils such that a particle will be stably levitated in this minimum as we show in Sec. VB. The double-loop trap has the advantage of a simple and straight-forward microfabrication process, since it can be fabricated with a single layer layout. Furthermore, the trap region is not restricted by the vertical separation between coils, unlike for the AHC-trap. A schematic of such a planar double-loop trap is shown in Fig. 1(d), which can be seen as a planar version of an AHC-trap. Fig. 1(e) shows a microfabricated double-loop trap from a 300 nm thick Nb film.

C. Superconducting properties of Nb films

We determined the superconducting properties of the 300 nm thick Nb film to have a $T_c \approx 9$ K, a critical current density up to $j_c = 5 \cdot 10^{11}$ A/m² and a critical field $B_{c2} \approx 0.4$ T, similar to values reported in literature^{37–39}. For the simulations in our work, we assume a current in the trap wires that corresponds to a current density of $1 \cdot 10^{11}$ A/m², which is below the critical current measured and, thus, leaves a safe margin for realistically running such a current through the trap. We model these wires as superconductors of finite extent, unless otherwise stated, with a thickness of 300 nm.

D. Fabrication of particles

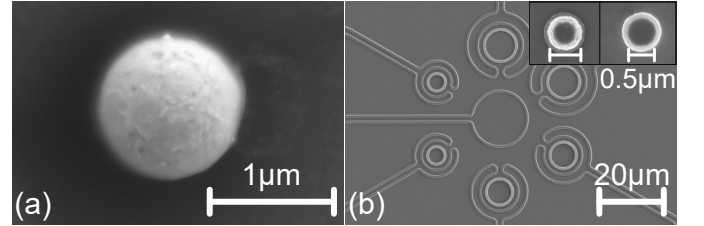


Figure 2. (a) SEM image of a Pb sphere on a silicon substrate. (b) Several double-loop traps of different dimensions each with an in-situ fabricated Nb ring. The insets in (b) show a Nb cylinder and ring on a Si substrate.

The particles can be obtained from metallic powders or can be microfabricated directly in the traps. Fig. 2(a) shows a spherical Pb particle individually selected from Pb powder. Note, however, that most particles in the powder are non-spherical and one has to pick-and-place the desired particles into the trap region. A systematic approach towards fabricating particles of well defined shapes can rely on etching of thin superconducting layers. Fig. 2(b) shows such an approach, where we fabricated cylinder- and ring-shaped particles from a Nb layer. The particles are fabricated by sputtering a 300 nm thick Nb layer on top of a sacrificial layer of hard-baked resist. The particle shape is patterned via EBL followed by ICP-RIE etching in the same way as the trap architectures. The sacrificial resist layer is removed using oxygen plasma, releasing the particles onto the substrate.

The trap fields we consider in the following remain below the first critical field of Nb (0.17 T) or of Pb

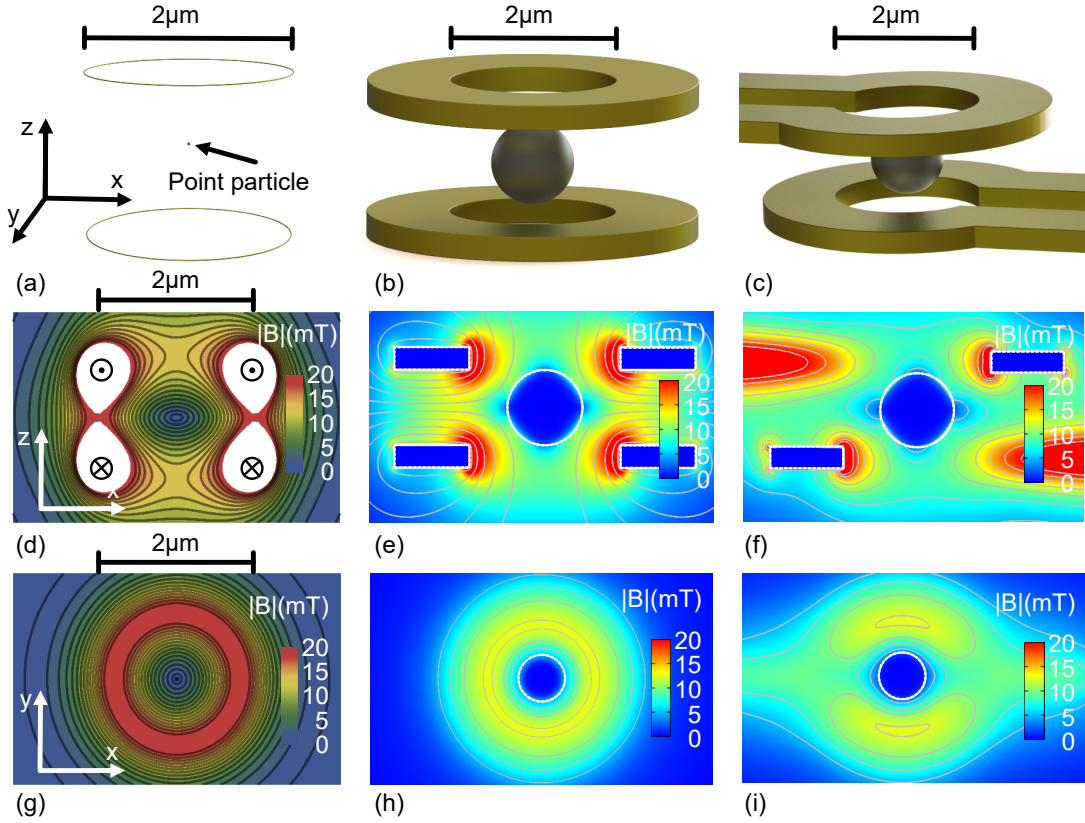


Figure 3. Schematic drawing of an AHC trap for calculations with the (a) point particle (empty trap), (b) FEM-2D and (c) FEM-3D models. The panels below show the corresponding field distributions for a cut in the XZ (d,e,f) and XY (g,h,i) planes that are tangent to the center of the trap. The white areas in (d) and red areas in (e,f) contain fields higher than the upper bound of the scale bar. Parameters used: inner coil diameter $2\text{ }\mu\text{m}$, outer coil diameter $4\text{ }\mu\text{m}$, coil separation $1\text{ }\mu\text{m}$, 30 mA applied current on each coil, $1\text{ }\mu\text{m}$ diameter superconducting sphere with $\lambda_L = 50\text{ nm}$ and $\rho = 8570\text{ kg/m}^3$. The chosen parameters are close to the values from Ref.⁵. For the FEM-2D simulations, we obtain trap gradients in the center of an empty trap of (9861, 9861, 19710) T/m along the (x, y, z) axes.

(0.08 T) on the particle surface in order to conform with our modeling assumption of levitating superconductors in the Meissner state, which is key to avoid undesired mechanical dissipation from moving flux vortices inside the particle^{5,8}.

V. MODELING OF CHIP-BASED SUPERCONDUCTING TRAPS

We model the properties of the superconducting traps using both analytical results and FEM simulations. A simplified analytic model assumes the coils to be one dimensional (1D) current loops and the superconducting object to be a *point particle* with an induced dipole moment, hence there is no dependence on the particle geometry. Analytical results can be derived for this simple case³⁰ and give a first indication about the trap properties. The image method²⁵ yields already much more accurate predictions, but assumes the particle to be a perfect *diamagnetic sphere* in a magnetic field distribution that is rotationally symmetric. Hofer et al.²³ de-

rived an analytic formula for the case of trapping a *superconducting sphere* in a quadrupole field, which uses as parameters the magnetic field gradient in the vertical direction, the radius of the superconducting particle and the penetration depth.

In general, one needs FEM simulations to account for deviations from symmetric field distributions and particle shapes. We consider different levels of realistic FEM modeling, which allows us to compare to the analytic models that idealize the trap geometry or neglect finite field penetration^{23,25,30}. *FEM-2D with 1D-wires* accounts for the volume of the superconducting particle and field penetration, but we assume that the magnetic field is generated by quasi 1D-closed loop coils, which are modeled with a cross section of $1 \times 1\text{ nm}^2$. This results in a rotationally symmetric geometry. A more realistic implementation called *FEM-2D* accounts for the volumes of the particle *and* the wires while still assuming that the coils are closed loops. The most realistic approach and the most computationally expensive called *FEM-3D* accounts for the symmetry breaking of the coil openings, which must be there to feed current into the

coils. FEM-3D simulations take typically between 100-600 GB of RAM and 30-120 minutes to solve on a computing cluster.

A. Anti-Helmholtz coil-trap

We first analyze the magnetic field distribution of a micrometer-sized, chip-based AHC trap. Fig. 3 shows the field distributions obtained via the analytic formula for an empty AHC [Fig. 3(d,g)], via FEM-2D [Fig. 3(e,h)] and via FEM-3D [Fig. 3(f,i)] for an AHC with a superconducting sphere. From the field distributions one observes that while there exist general similarities between the predictions of each model, the differences between them are also significant. Most importantly, the magnitude of the magnetic field and its distribution change, which affect the trap frequency and levitation point as we discuss in the following.

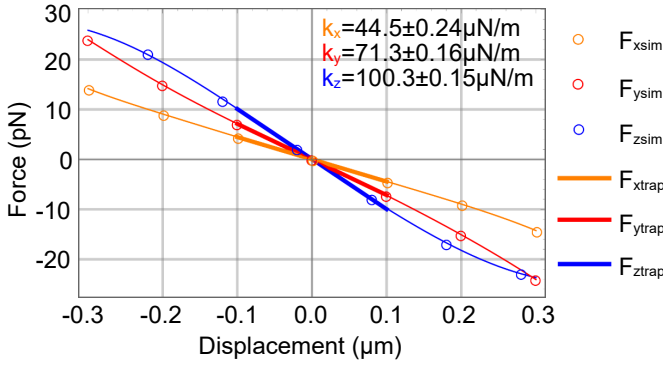


Figure 4. Force acting on a $1\mu\text{m}$ diameter spherical particle in the AHC-trap considered in Fig. 3(c,f,i) as a function of the particle's displacement relative to the center of the AHC-trap in the x, y, z directions. Open circles show the FEM-3D simulation results, the thin solid line is a guide to the eye and the thick solid line represents a linear fit, from which the restoring constant k_i and its uncertainty is calculated.

a. Trap stability for translational degrees of freedom

A stably levitated particle experiences a restoring force for all translational degrees of freedom. Fig. 4 shows the total force acting on a superconducting sphere close to the center of the AHC-trap. The force is calculated as explained in Appendix E from the magnetic field distributions shown in Fig. 3(f,i). At the center of the trap, the force equals zero as the magnetic levitation force and the gravitational force balance each other. The negative gradient of the force corresponds to a restoring force pushing the particle back to the trap center for small displacements. Thus, this parameter set results in a stably levitated particle. The thick solid lines are linear fits within $\pm 100\text{nm}$ of the trap position from which the restoring constants k_i and, thus, trap frequencies ω_i are calculated, see Eq. (7). In the following, we use the uncertainty of the linear fit on k for calculating the uncertainty of the trap frequency.

b. *Trap stability for angular degrees of freedom* For any non-spherical particle, the magnetic field distribution can result in a torque, which will align the particle in the field until its potential energy is minimized. Hence, just as there is a trap center for the translational degrees of freedom, there is a stable particle orientation for the angular degrees of freedom. The torque τ acting on the particle is calculated as detailed in Appendix E. The torque restores the particle to the stable orientation with a spring constant k_i^τ given by:

$$k_i^\tau = -\frac{\partial \tau_i}{\partial \theta_j} \quad (9)$$

where τ_i is the torque component w.r.t. rotation around the x (y) axis and θ_j is the particle tilt with respect to the y (x) axis.

In the following we consider the torque acting on a cylinder or a ring levitated in an realistic AHC-trap. Fig. 5 shows the x and y components of the torque versus the inclination of the particle with respect to the other axis. Equilibrium orientations are found when the torque is zero and its slope is negative. From the orientations fulfilling these conditions, the one with the largest slope is the stable orientation, while the others will be metastable. The stable and a metastable orientation for a cylinder are 0 and $\pi/2$ tilt with respect to the y axis, respectively. For the orientation with respect to the x axis, the stable orientation is close to 0, with a slight shift in angle due to the coil openings. For a ring with zero trapped flux the stable and metastable orientations are at 0 and $\pi/2$ tilt with respect to the y-axis, respectively. However, for the orientation with respect to the x-axis, there is only one stable orientation close to $\pi/6$. This asymmetry is caused by the coil openings and flux quantization in the ring hole, which generates an extra current that increases the energy of the system. Hence, a torque that works to minimize the current in the ring will appear, orienting it towards the coil openings, where the field is weaker. If the AHC-trap had no openings, such as the one shown in Fig. 3(b), the stable and a metastable orientation would appear at 0 and $\pi/2$ with respect to the y-axis, respectively. Note that the torque acting on the ring is approximately one order of magnitude larger than that on the cylinder.

c. *Trap frequency* Tab. I shows the obtained trap frequencies of the three particle shapes, sphere, cylinder and ring, all with the same diameter, for a specific set of parameters, cf. with Ref.⁹. There is some general behavior observable. First, when accounting for the volume of the particle and treating it as a superconductor in the Meissner state instead of a perfect diamagnet (i.e. when comparing the point particle or image method to superconducting particle, FEM-2D and FEM-3D), the magnetic field gradient around the particle is smoothed, thus, decreasing the trap frequency. Second, accounting for the volume of the coils and their openings spreads out the magnetic field, decreasing its gradient at the trap po-

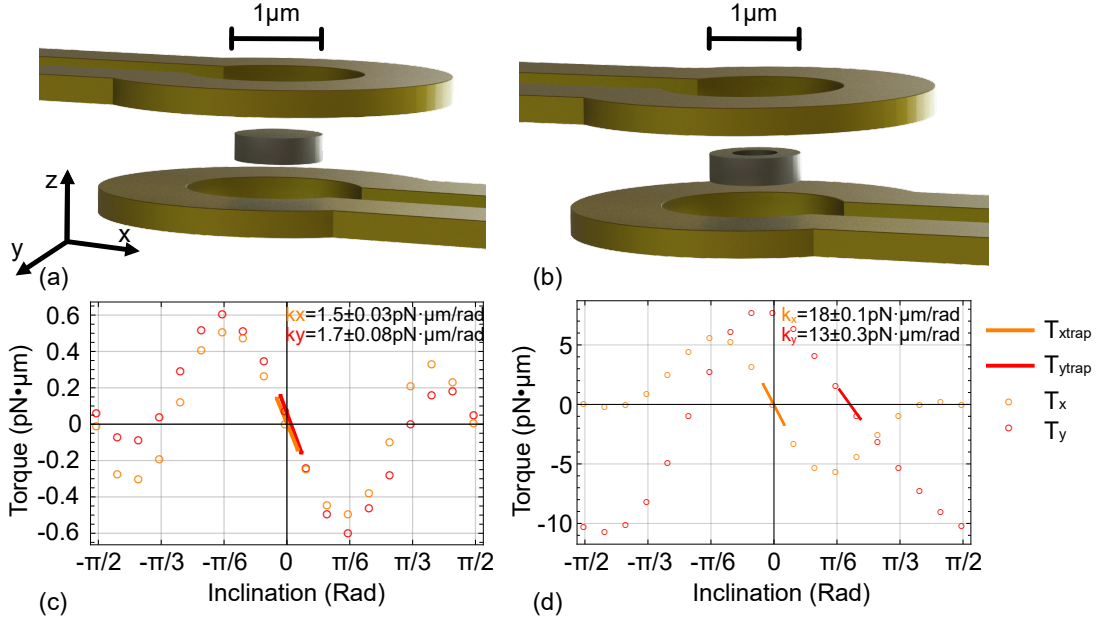


Figure 5. Schematic representations of a (a) cylinder and (b) ring trapped in a realistic AHC-trap. Panels (c) and (d) show the FEM-3D simulation results of the x (orange) component of the torque versus the particle tilt with respect to the y axis, and the y (red) component of the torque versus the particle tilt with respect to the x axis. Zero tilt is defined by the particle orientation as shown in (a,b). Parameters are the same as in Fig. 3 for the AHC trap and Tab. I for the particles. The corresponding angular frequencies $\omega_i^T = \sqrt{k_i^T/I}$ with I being the moment of inertia are (c) $\omega_x^T = (14.0 \pm 0.15)$ kHz and $\omega_y^T = (15.0 \pm 0.35)$ kHz for the cylinder, and (d) $\omega_x^T = (60.0 \pm 0.17)$ kHz and $\omega_y^T = (52.1 \pm 0.52)$ kHz for the ring.

Method	Sphere $\omega_{x,y,z}/2\pi$ (kHz)	Cylinder $\omega_{x,y,z}/2\pi$ (kHz)	Ring $\omega_{x,y,z}/2\pi$ (kHz)
Point particle	(24.8, 24.8, 49.6)	—	—
Diamagnetic particle	(—, —, 45.7)	—	—
Superconducting particle	(18.2, 18.2, 36.5)	—	—
FEM-2D [3D]	[[17.8], [17.8], 28.6]	[[16.6], [16.6], 47.5]	[[26.4], [26.4], 49.1]
FEM-3D	(15.8, 19.9, 23.8)	(12.6, 17.2, 36.8)	(25.4, 26.8, 37.9)

Table I. Trap frequencies in an AHC trap for levitating particles of different shape: a sphere of 1 μm diameter, a cylinder of 1 μm diameter and 300 nm height, and a ring with 300 nm thickness and inner and outer diameters of 0.5 μm and 1 μm , respectively. Other parameters of the trap as in Fig. 3. Note that trap frequencies along the x and y directions for the case FEM-2D were actually simulated using FEM-3D and a symmetric trap. The uncertainties for the frequencies for the (sphere, cylinder, ring) are below (0.14%, 0.13%, 0.13%) for FEM-2D and (0.7%, 1.3%, 0.5%) for FEM-3D.

sition, thus, leading to different trap frequencies in the x and y directions (FEM-2D vs. FEM-3D) and smaller frequencies along z.

Particles of non-spherical shape result in higher trap frequencies for the z axis. The difference in trap frequency can be attributed to a great extent to the different mass m of the particles as $\omega_i \propto \sqrt{1/m}$. Additionally, the spring constants k for the different particles are also different due to the varying demagnetizing effects (cf. Appendix B 2), which result in a locally varying magnetic field distribution close to the particle surface.

Different trap and particle sizes have a systematic effect on the trap frequency. We first consider the dependence of the trap frequency on the particle size in a trap with unaltered dimensions. In Fig. 6(a) we ob-

serve that for large particles the image method gives similar results as FEM-2D with 1D-wires, since the normal conducting volume fraction of the particle is negligible compared to its superconducting volume fraction and the trap wires are quasi one-dimensional. Deviations occur when the particle radius is decreased to a size that magnetic field penetration becomes relevant, i.e., for $\lambda_L/R_{\text{sphere}} \gtrsim 0.1$. When comparing FEM-2D with 1D-wires to a superconducting particle in a quadrupole field²³, we observe that for small particle sizes the FEM simulation gives similar results. However, for larger particle sizes ($\lambda_L/R_{\text{sphere}} \lesssim 0.15$), the two methods give different results, which we attribute to the difference between a quadrupole field and the real field generated by the wires, which becomes more pronounced for larger

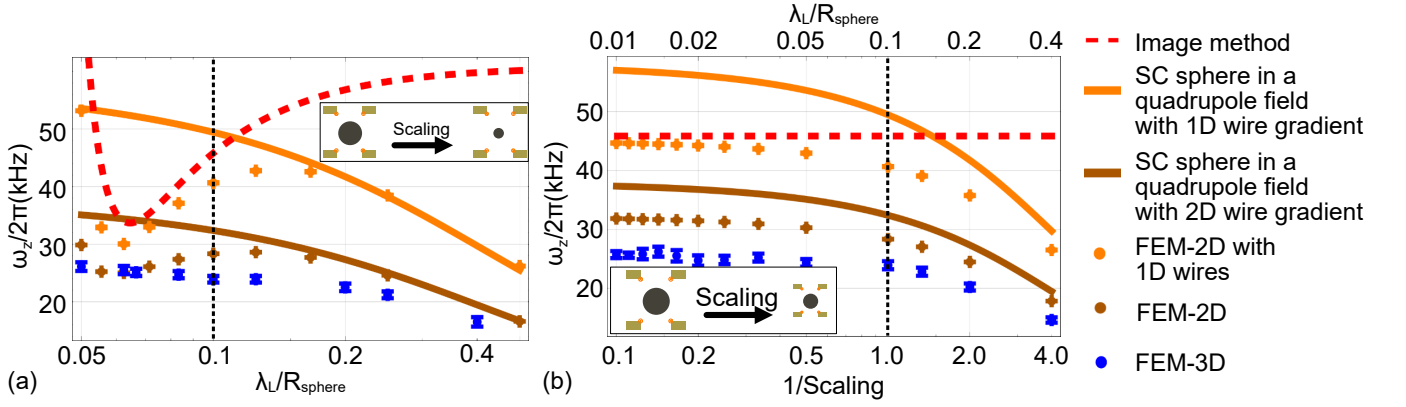


Figure 6. Vertical trap frequency of a superconducting sphere trapped in a realistic AHC predicted by the image method²⁵, by assuming a superconducting sphere in a quadrupole field²³, FEM-2D with 1D-wires, FEM-2D and FEM-3D. (a) The radius of the particle is scaled and the geometrical parameters of the trap and λ_L are kept constant with parameters as given in Tab. I. (b) The geometrical parameters of the trap and particle are taken from Tab. I and scaled by a scaling factor while the current density in the coils and λ_L are kept constant. The vertical dotted black lines indicate the initial geometry. The orange points in the insets indicate the location of the current loops when calculating the trap frequency using the image method and FEM-2D with 1D-wires. In Appendix D we also consider the case when the current loops are centered within the wire.

particles. When accounting for coils of finite extent via FEM-2D, the gradient of the field decreases compared to FEM-2D with 1D-wires, thus decreasing the trap frequency. Also in this case, assuming a superconducting sphere in a quadrupole field gives similar results for small particle sizes, but deviates for larger ones. When accounting for the opening of the trap wires via FEM-3D, the trap frequency further decreases, which yields the most realistic prediction.

We now consider scaling of the AHC-trap by scaling the trap geometry with a factor such that the dimensions of sphere and trap are simultaneously changing size, while keeping the current density in the coils and λ_L constant, see Fig. 6(b). For large geometries, i.e., negligibly small penetration depths, the image method is in agreement with FEM-2D with 1D-wires, as in Fig. 6(a). The decrease of the trap frequency for FEM-2D with 1D-wires when scaling down the system (i.e. for scaling factors $\lesssim 3$, i.e., $1/\text{scaling factor} \gtrsim 0.3$) is due to the fact that for particles with a radius approaching λ_L , a significant portion of the sphere's volume becomes a normal conductor. This volume does not contribute strongly to the magnetic energy. Thus, the magnetic force on the particle weakens, which decreases the trap frequency, leading to the difference between the image method and FEM-2D with 1D-wires. As before, when modeling the finite extent of the wires via FEM-2D the trap frequency decreases compared to 1D modeling of the wires. For a superconducting sphere in a quadrupole field, we get similar results for small geometries, but deviations for large geometries. We attribute this behaviour as in Fig. 6(a) to the deviation of the real field of the trap from a quadrupole field in the case for larger geometries. When incorporating the coil opening via FEM-3D, the trap frequency is further reduced, which corresponds to the most realistic situation.

Levitation of a ring is particularly interesting. Fig. 7 shows the dependence of trap frequency for the amount of trapped flux, Φ_t , in the ring for an AHC trap with 100 mA of current (corresponding to increasing j_c to $3.3 \cdot 10^{11} \text{ A/m}^2$). Strikingly, the trap frequency decreases with increasing number of trapped Φ_t , regardless of its orientation. The levitation height, however, increases monotonously with Φ_t . This is because the ring seeks the region in the trap with a magnetic field strength that will generate the same flux as Φ_t . As a result, the ring gets closer to one coil or the other depending on the orientation of Φ_t , and, thus, further away from the trap center, where the field gradient is highest, reducing the trap frequency. Note, that if the trap does not generate a high enough magnetic field, a ring with non-zero number of trapped flux quanta will be ejected from the trap.

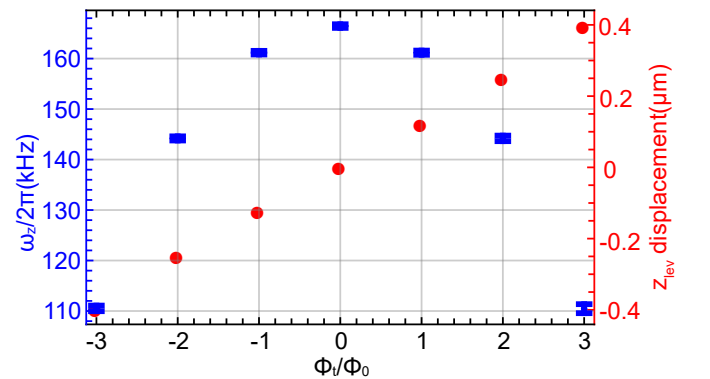


Figure 7. Vertical trap frequency and levitation height with respect to the center of the trap as a function of trapped flux in a levitated superconducting ring in an AHC-trap. Parameters as in Tab. I, but with an increased current in the coil wires to 100 mA. Simulated using FEM-2D.

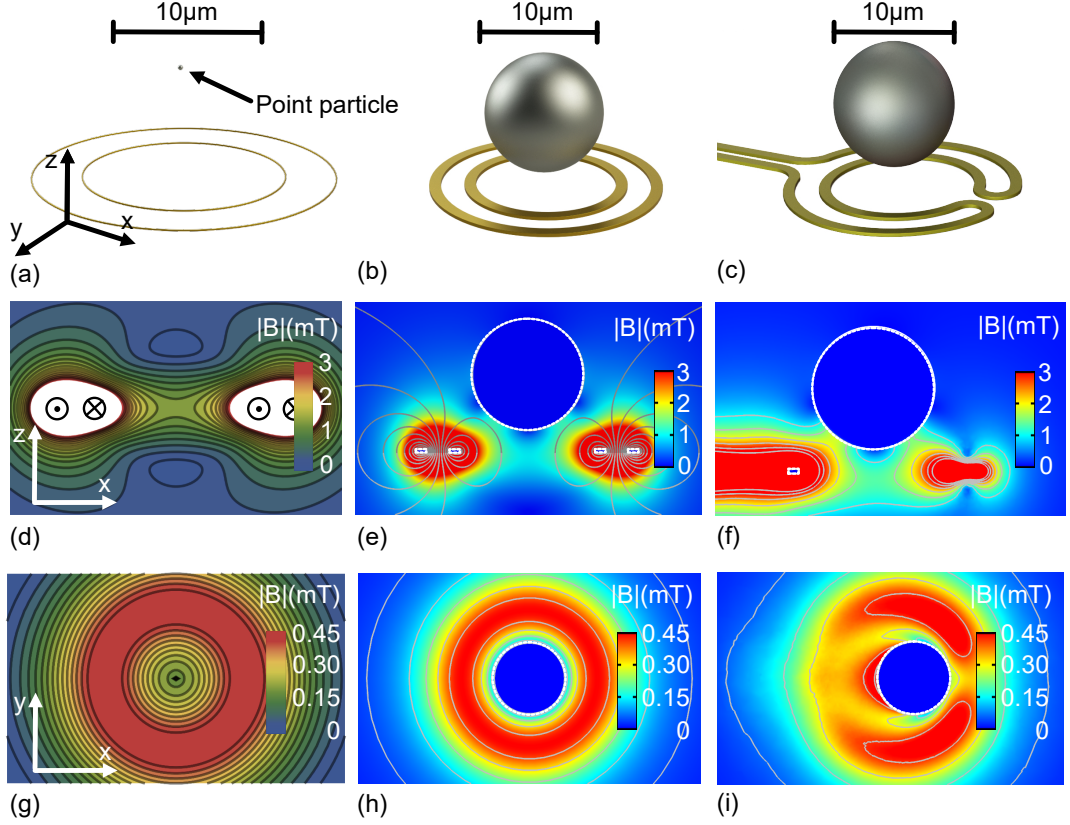


Figure 8. Schematic representations of a double-loop trap for the (a) point particle (empty trap), (b) FEM-2D and (c) FEM-3D models and their corresponding field distributions for a cut in the XZ (d,e,f) and XY (g,h,i) plane that are tangent to the center of the trap. The white areas in (d) and red areas in (e,f,g,h) contain fields higher than the upper bound of the scale bar. Parameters: inner coil diameter $12\mu\text{m}$, outer coil diameter $18\mu\text{m}$, applied current 38 mA , $10\mu\text{m}$ diameter superconducting sphere with $\lambda_L = 50\text{ nm}$ and $\rho = 8570\text{ kg/m}^2$. For the FEM-2D simulations, we obtain trap gradients in the trap center of an empty trap of $(65, 65, 125)\text{ T/m}$ along the (x, y, z) axes.

B. Double-loop trap

We now turn to modeling the trap properties of the double-loop trap using the different models presented before.

a. Trap stability The simple layout of the double-loop trap comes at the expense of sacrificing magnetic field gradient and intensity. To illustrate this, we show the magnetic field distributions for such a trap in Fig. 8. In Fig. 8(d,g) the trap region is visible as the region of the surface plot surrounded by high field intensity. As can be seen in Fig. 8(e,f,h,i) a particle with a diameter similar to the trap size will fill up the trap region and is stable in the z direction due to gravity, since there is no magnetic field from above pushing it down. For these particle sizes, the double-loop trap is magneto-gravitational.

Just as for the AHC-trap, the breaking of symmetry due to the openings of the coils has a significant effect in the double-loop trap. As shown in Fig. 8(i), the field at the opening of the coil on the side of the current feed lines interferes constructively with the field generated by the inner coil, creating a higher field intensity at the left

side of the particle that pushes it towards the direction of positive x . At the same time, the field opening at the opposite side weakens the field, creating a lower field intensity at the right side of the particle, which weakens the push in the direction of negative x towards the coil center. These two factors combined weaken the restoring force along the x -axis, which can potentially lead to the particle not being trapped. Thus, a careful design of the double-loop trap is required in order to achieve stable levitation. As a rule of thumb, the opening left between the wires should be smaller than the wire width of the coil. The trap center position is displaced from the coil center towards the opening, and the trap frequency along that direction is smaller than for any other in-plane direction.

b. Trap frequency Tab. II shows trap frequencies for a $10\mu\text{m}$ spherical particle in a double-loop trap. The frequencies are below 1 kHz and, compared to the AHC trap, rather low, due to the double-loop trap being magneto-gravitational for this particle size. Note, the trap frequency will not change considerably for particles of different shapes, since any increase of the field gradient around the particle will push it higher up into regions of smaller magnetic field and, thus, smaller trap frequency.

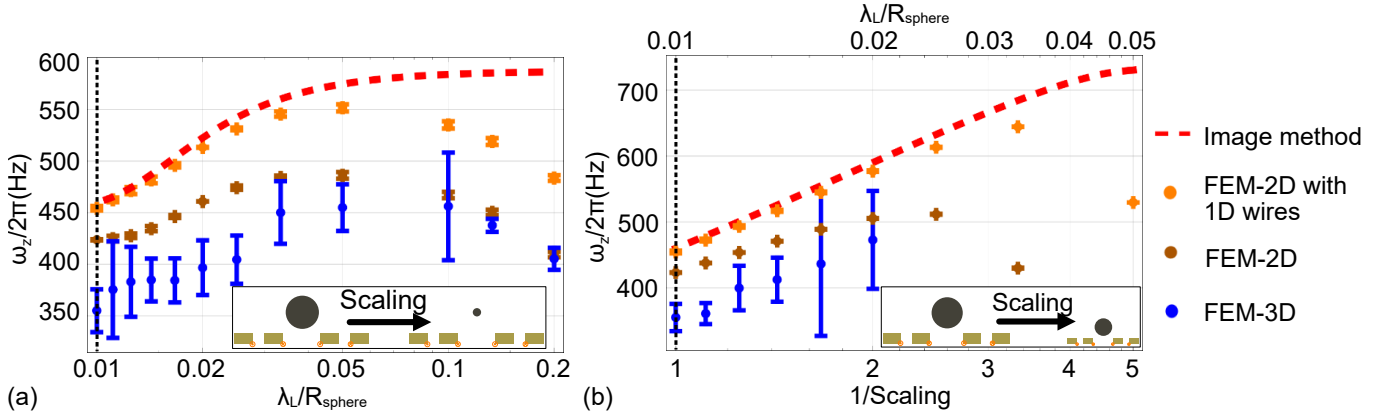


Figure 9. Vertical trap frequency dependence of a superconducting sphere trapped in a realistic double-loop trap predicted by the image method²⁵, FEM-2D with 1D-wires, FEM-2D and FEM-3D. (a) The radius of the particle is scaled and the geometrical parameters of the trap are kept constant to the ones in Fig. 8. (b) The geometrical parameters of the trap and the particle are taken from Fig. 8 and scaled by a scaling factor while the current density in the coils and λ_L are kept constant. The vertical black dotted lines indicate the initial geometry. The orange points in the insets indicate the location of the current loops when calculating the trap frequency using the image method and FEM-2D with 1D-wires. In Appendix D we also consider the case of current loops centered within the wire.

Method	$\frac{\omega_x}{2\pi}$	$\frac{\omega_y}{2\pi}$	$\frac{\omega_z}{2\pi}$
Point particle	149.8	149.8	524.4
Diamagnetic particle	–	–	465.1
FEM-2D [3D]	[113.3]	[113.3]	455.2
FEM-3D	82.3	119.8	355.0

Table II. Trap frequencies for a $10\mu\text{m}$ sphere levitated in a double-loop trap. Parameters as in Fig. 8. All units are Hz. The uncertainties for the trap frequencies are below 0.7% for FEM-2D and 8.7% for FEM-3D. Note that trap frequencies along the x and y directions for the case FEM-2D were actually simulated using FEM-3D and a symmetric trap.

In the following, we look at systematic effects on the trap frequency. We first consider a particle with different size in a trap with unaltered dimensions in Fig. 9(a). For large particles, FEM-2D with 1D-wires agrees with the image method, while it deviates for smaller particles due to the finite field penetration accounted for in FEM. Modeling via FEM-2D and FEM-3D results in gradually smaller trap frequencies due to a reduced gradient of the trap. Interestingly, the trap frequency reaches a maximum around $\lambda_L/R_{\text{sphere}} \sim 0.05$. For larger particles, the trap frequency decreases due to the trap becoming more magneto-gravitational, whereas for smaller particle sizes the magnetic field penetration into the particle reduces the trap frequency.

In Fig. 9(b) we consider a scaled system, where both the trap and the particle change size with a scaling factor while keeping the current density of the trap and λ_L constant. Again, we find agreement between the image method and the FEM-2D with 1D-wires for large geometries and an increasing discrepancy for smaller geometries due to increasing field penetration, as discussed before. Smaller geometries than the ones considered for

each method, are not capable of levitation because the magnetic lift force does not overcome the weight of the particle. When modeling via FEM-2D the trap frequency decreases due to reducing the field gradient and further decreases when modeling via FEM-3D due to accounting for the wire opening, yielding the most realistic prediction.

VI. FLUX-BASED READ-OUT OF LEVITATED PARTICLE MOTION

A major motivation for undertaking magnetic levitation of superconducting micrometer-sized objects is the exceptional decoupling of the levitated object from its environment^{5,6}. To verify this decoupling experimentally, one needs to detect the motion of the levitated particle. Motion detection can rely on flux-based read-out via a pick-up coil placed in the vicinity of the trap^{9,14}. Then, particle oscillations around the trap center generate perturbations in the magnetic field distribution, which translate into a change of the magnetic flux threading through a pick-up coil. The pick-up coil could, in turn, be connected to a DC-SQUID, which converts the flux signal into a measurable voltage signal. The expected signal in a pick-up loop has been calculated in previous work for the case of idealized situations^{5,9}.

Using FEM, we can now calculate the expected signal for realistic geometries by accounting for extended volumes and flux quantization. In the following, we consider a $1\mu\text{m}$ diameter spherical particle trapped in an AHC-trap (cf. Fig. 3). We are interested in the magnetic flux threading a pick-up coil (shaded area in Fig. 10(a)) for different particle displacements with respect to the trap center. We show in Fig. 10(b) that our model predicts

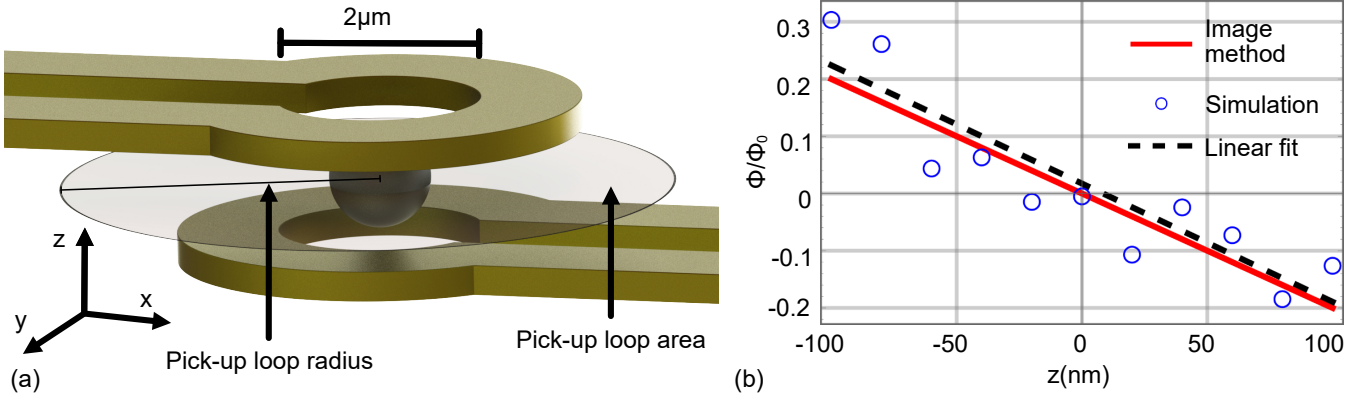


Figure 10. Flux-based mechanical motion detection simulated via FEM-3D. (a) Schematic representation of the trap arrangement. The grey area represents the area over which the magnetic flux is integrated. (b) The flux threading through the grey area as a function of the particle displacement. Parameters as in Tab. I.

	Sphere	Cylinder	Ring
$\eta_{x,y,z}$ ($\mu\phi_0/\text{nm}$)	$(5.4, 6.4, 20.6) \cdot 10^2$	$(9.0, 1.1, 7.1) \cdot 10^2$	$(8.9, 0.05, 10.1) \cdot 10^2$
$S_{\phi_{x,y,z}}$ ($\mu\phi_0/\sqrt{\text{Hz}}$)	$(5.8, 5.1, 12.5) \cdot 10^3$	$(20.6, 1.6, 3.2) \cdot 10^3$	$(8.9, 0.05, 4.9) \cdot 10^3$
$S_{\phi_{0x,0y,0z}}$ ($\mu\phi_0/\sqrt{\text{Hz}}$)	(1.8, 1.7, 4.7)	(5.7, 0.5, 1.5)	(3.4, 0.02, 2.4)

Table III. Signal strength η_i and noise power spectral density S_{ϕ_i} on resonance detected by a pick-up coil with radius of 2 μm located between the two coils of an AHC-trap. The dimensions of the trap and area of the pick-up coil are shown in Fig. 10(a). The trap and particle parameters are the same as in Tab. I. $S_{\phi_{x,y,z}}$ ($S_{\phi_{0x,0y,0z}}$) denotes the signal assuming a Q of 10^7 and a temperature of 4 K (quantum ground state). The uncertainties are below 25% for the z direction and around 50% for x and y directions.

magnetic flux changes similar to the ones of the analytical expressions for a perfect diamagnetic sphere in a quadrupole field⁵.

The slope of the curve in Fig. 10(b) yields the signal strength per displacement along direction i as (normalized by $10^{-6}\phi_0 = 1\mu\phi_0$):

$$\eta_i = \frac{1}{\mu\phi_0} \frac{\partial \Phi}{\partial x_i}. \quad (10)$$

Commonly, one measures the flux noise power spectral density $S_{\phi_i}(\omega)$, which is given as⁴⁰:

$$S_{\phi_i}(\omega) = \eta_i S_{x_i}(\omega) = \eta_i x_{\text{rms},i} \sqrt{\frac{\gamma_i}{(\omega - \omega_i)^2 + \gamma_i^2}}, \quad (11)$$

with $S_{x_i}(\omega)$ is the noise power spectral density of mechanical motion, $x_{\text{rms},i}$ the root mean square amplitude of the oscillation in direction i (cf. Eq. (8)) and $\gamma_i = \omega_i/Q_i$ is the mechanical damping with Q_i being the mechanical quality factor. On mechanical resonance, one obtains

$$S_{\phi_i}(\omega_i) = \eta_i x_{\text{rms},i} / \sqrt{\gamma_i}. \quad (12)$$

Tab. III shows η_i and $S_{\phi_i}(\omega_i)$ for a sphere, cylinder and ring in an AHC-trap at a temperature of 4 K and for a conservative^{5,6} $Q = 10^7$. We also consider the case of detecting the ground state motion, i.e., $x_{0,i} = \sqrt{\hbar/m\omega_i}$, via measurement of flux, $S_{\phi_{0i}}(\omega_i) = \eta_i x_{0,i} / \sqrt{\gamma_i}$.

The simulated signals are on the order of $10^3 \mu\phi_0/\sqrt{\text{Hz}}$ for thermally driven motion and some $\mu\phi_0/\sqrt{\text{Hz}}$ for ground state motion. The former signals are well above the noise floor of state-of-the-art SQUID sensors ($< 1 \mu\phi_0/\sqrt{\text{Hz}}$ for detection frequencies above 1 kHz^{41–43}). While detection of ground state motion seems feasible, a further decrease in mechanical damping γ_i would be beneficial, as is predicted by theory^{5,9}.

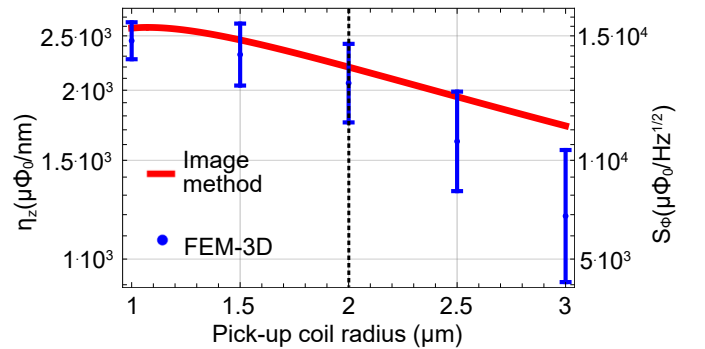


Figure 11. Comparison of the signal strength η_i and power spectral density S_{ϕ_i} detected by a pick-up loop of varying radius placed between the two coils of an AHC trap. We consider the same trap as the one in Fig. 10. The dashed line indicates the size of the pick-up loop as used in Tab. III.

Fig. 11 shows the signal strength and noise power spectral density when varying the pick-up coil radius. For

small radii, the FEM results match within their uncertainty the value predicted by the image method, but slightly deviate for larger radii. This is because as the radius of the pick-up loop grows, the FEM model integrates over more coarsely meshed regions of the model and numerical errors accumulate.

VII. CONCLUSIONS

In conclusion, we have used FEM modeling for simulating realistic type I superconducting structures in the Meissner state including flux quantization. We have based our modeling on the \mathbf{A} - V formulation for implementing the Maxwell-London equations, which uses only a single parameter, the London penetration depth λ_L .

We applied this modeling technique in the context of chip-based superconducting levitation of micrometer-sized particles to analyze in detail two trap architectures. Crucially, we have shown that trap properties, like trap stability and frequency, differ from idealized models due to breaking of symmetry by coil openings, demagnetizing effects and flux quantization. Our FEM-based simulations incorporate these effects and, thus, allow for a careful design of realistic trap architectures. We predict large trap frequencies in the 40 kHz range for ring-like particles trapped in a micrometer-sized AHC-trap compared to a couple of hundred Hz for a similar sized planar double-loop trap. We have demonstrated how to fabricate such traps and particles from thin Nb films.

Large trap frequencies are beneficial for reducing the impact of environmental vibrational noise on particle motion, both from the seismic background⁴⁴ as well as from the vibrational noise coming from the utilized cryostats necessary for cooling superconductors^{45,46}. A lower vibrational background noise results in a smaller vibration-induced heating rate of particle motion, which is beneficial for follow-up experiments targeting motional quantum ground state cooling of levitated particles^{5,6}. Further, we have shown that for realistic trap geometries the motion of the particle in the trap can be measured by state-of-the-art SQUIDs, whose measurement signal would be used as feedback signal for performing feedback cooling of particle motion.

Including flux pinning in our modeling^{47–49} via, for example, the critical state model³³ would allow studying alternative trap opportunities, which may offer chip-based traps with even higher trap frequencies. Our modeling is generic and applicable not only in the present context of simulating chip-based superconducting traps for quantum or sensing experiments, but also for designing superconducting magnetic shields⁵⁰ or filling factors in superconducting resonators³², when considering superconductors in the Meissner state.

ACKNOWLEDGMENTS

We acknowledge fruitful discussions with Jordi Prat Camps, Prasanna Venkatesh and COMSOL support. We thank Carles Navau and Àlvàr Sanchez for a critical reading of the manuscript. We are thankful for initial support in microfabrication from David Niepce. The work was supported in part by *Chalmers' Excellence Initiative Nano* and the *Knut and Alice Wallenberg Foundation*. Sample fabrication was performed in the Myfab Nanofabrication Laboratory at Chalmers. Simulations were performed on resources provided by the Swedish National Infrastructure for Computing (SNIC) at C3SE, Chalmers, partially funded by the Swedish Research Council through grant agreement no. 2016-07213.

Appendix A: Working principle of the model

Our modeling is based on the \mathbf{A} - V formulation^{28,29}, which is to solve the Maxwell equations using the magnetic vector potential \mathbf{A} and the voltage V as the dependent variables. Alternative methods to model superconductors in 3D are based on the \mathbf{T} - Ω formulation, that treat the current vector potential \mathbf{T} and the magnetic scalar potential Ω as the dependent variables²⁹.

There are a few practical differences between these two formulations. While they both have the same number of dependent variables in three dimensions, \mathbf{T} - Ω formulation relies on an additional equation known as the power law, which relates the electric field and the current density:

$$|\mathbf{E}| = E_c \left(\frac{|\mathbf{J}|}{J_c} \right)^n, \quad (\text{A1})$$

with the experimentally determined parameters n , E_c and J_c , where the latter two are the critical electric field and critical current density, respectively. Despite of the greater number of equations, \mathbf{T} - Ω formulation is shown to achieve convergence more easily than \mathbf{A} - V formulation. This is because Eq. (A1) is much easier to compute than $\mathbf{J}(E)$ for a superconductor, due to the electrical conductivity of the superconductor being highly non-linear. Furthermore, in \mathbf{A} - V formulation, \mathbf{A} needs to be differentiated as a discrete variable, which is not an easy task numerically and complicates achieving convergence further²⁸.

On the other hand, \mathbf{A} - V formulation has its advantages. It has less equations to solve, and thus, the system matrices are smaller so less memory is required. It uses a single, and well known, experimental parameter, namely λ_L , instead of three parameters required in the \mathbf{T} - Ω formulation that aren't necessarily available for all materials. It is much simpler to model magnetized objects, superconductors, coils and externally applied magnetic fields using \mathbf{A} and V as variables, as it requires very few

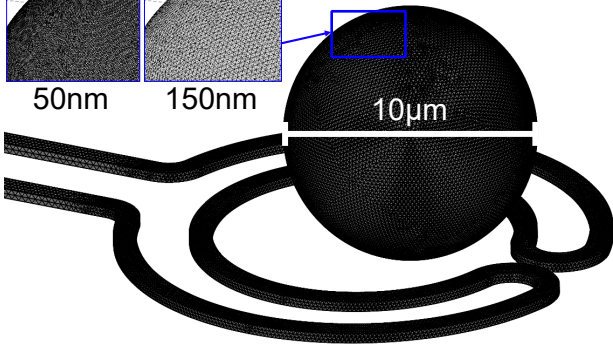


Figure 12. Surface mesh of a superconducting sphere and a double-loop trap. The element size has been increased three-fold (to 150 nm in the figure) for the sake of visibility. Parameters as in Fig. 8. The insets show a magnified image of the surface mesh of the sphere with the same exaggerated surface mesh element size as the full image (150 nm) and the one used in the FEM-3D simulations (50 nm).

and relatively simple modifications of FEM software to do so. And finally, while achieving convergence is still more challenging than with the $\mathbf{T}\text{-}\Omega$ formulation, the use of quasi-static equations (i.e. no time dependence) further simplifies the equations of the system. Furthermore, the tools that current FEM solvers offer, such as multigrids, control over tolerance and divergence cleaning techniques, make simulations arguably less time consuming than performing the experiments to determine the parameters required for the $\mathbf{T}\text{-}\Omega$ formulation.

With that in mind, there are a couple of important things to consider when using FEM modeling for magnetic field distributions around superconducting structures. The mesh needs to be constructed very carefully in the regions close to the superconducting surfaces and regions with high magnetic field density and gradient, see as an example Fig. 12 and the detailed discussion in Appendix C. This has to do with the characteristic length scales of superconductors and field gradients in such systems, rather than the method we use to compute them. The magnetic field, current density and thus the magnetic forces on the superconductor are mainly determined by the regions of high magnetic field gradient, which in turn are closely related to demagnetizing effects and the field expulsion of the superconductor. Thus, to obtain valid results the meshing around the surfaces of the superconducting objects needs to be very dense, on the order of or better than λ_L , which can become computationally demanding. Furthermore, we need to consider that the magnetic field is gauge invariant. If the initial values for the magnetic vector potential are numerically too large or too small, they can become too hard to compute numerically and the system will not converge. Thus, especially when high values of \mathbf{B} are involved, a guess within a few orders of magnitude for \mathbf{A} is required for the software to converge. Alternatively, gauge fixing for \mathbf{A} can be used if the software allows such possibility.

Appendix B: Validation of FEM modeling

In order to validate our model with test cases, we compare the results it yields to the predictions made by analytical equations. The cases used for validation are (i) the magnetic field expulsion of a superconductor and (ii) demagnetizing effects of superconducting objects with different geometries. We also look at flux quantization in a ring and calculate the torque acting on a ring in a homogeneous magnetic field.

1. Magnetic Field Expulsion

To examine magnetic field expulsion we consider (i) a flat superconducting object with infinite extension in the z and positive x axes and (ii) a superconducting thin film with infinite extension in the z axis, under a homogeneous magnetic field $\mathbf{B}_0 = B_0 \cdot \mathbf{e}_z$, see Fig. 13. For the first case, the Maxwell-London equations predict that \mathbf{B}_0 is expected to decay exponentially within the superconductor with the characteristic length scale λ_L (for superconductors with sizes $\gg \lambda_L$)³¹:

$$\mathbf{B}(x) = \left(0, 0, B_0 e^{-\frac{x}{\lambda_L}}\right)^T, \quad (\text{B1})$$

where x is the distance from the superconductor's surface. For the second case, the magnetic field inside a superconducting thin film of thickness t is expected to also decay exponentially from both sides, but the tails of each exponential will overlap in the middle of the thin film, thus limiting the field expulsion³¹:

$$\mathbf{B}(x) = \left(0, 0, B_0 \frac{\cosh\left(\frac{x}{\lambda_L}\right)}{\cosh\left(\frac{t}{2\lambda_L}\right)}\right)^T. \quad (\text{B2})$$

We simulate the structures for case (i) with a semi-infinite superconductor that occupies the positive half space $x > 0$ and all z , and for case (ii) with a superconducting thin film with $t = 1 \mu\text{m}$ in x direction centered at zero while $y = z = \infty$. In both cases, we use $\lambda_L = 100 \text{ nm}$ and a homogeneous magnetic field $\mathbf{B}_0 = B_0 \cdot \mathbf{e}_z$ with $B_0 = 100 \text{ mT}$ applied parallel to the z axis. The results are shown in Fig. 13(c,d) and show excellent agreement between FEM modeling and analytical equations.

2. Demagnetizing Effects

Field expulsion concentrates field lines around the surfaces of the superconducting object parallel to the field. In these regions, an increase of magnetic field intensity appears. This increase can be calculated analytically as a multiplying factor called demagnetizing factor.

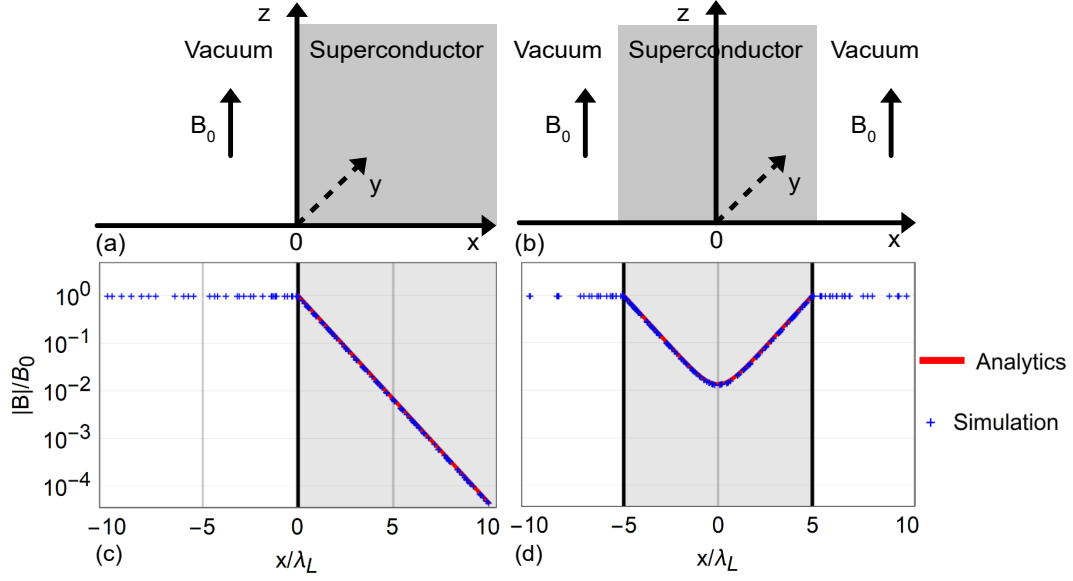


Figure 13. Magnetic field expulsion predicted by analytical equations (red line) and simulations (blue crosses) for (a) a semi-infinite superconductor and (b) a $t = 1 \mu\text{m}$ thin film superconductor. The grey shaded areas represent the superconducting domain. The simulation points are unevenly spaced due to the mesh of the model being finer at the vacuum-superconductor interface. Parameters used are: $\lambda_L = 100 \text{ nm}$, $\mathbf{B}_0 = B_0 \cdot \mathbf{e}_z$ with $B_0 = 100 \text{ mT}$.

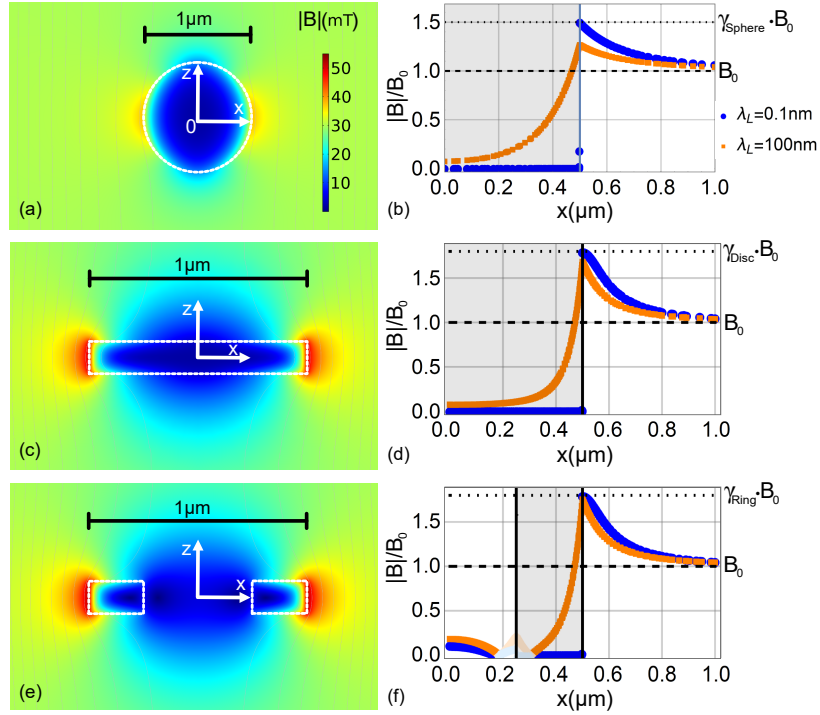


Figure 14. Magnetic field distributions around a superconducting (a) sphere, (c) cylinder and (e) ring under an external magnetic field $\mathbf{B}_0 = B_0 \cdot \mathbf{e}_z$ with $B_0 = 30 \text{ mT}$. Panels (b,d,f) show the magnetic field intensity along the x -axis for a nearly perfect diamagnet ($\lambda_L \approx 0$) and a superconductor ($\lambda_L = 100 \text{ nm}$). The black dashed line indicates the modulus of the applied field $|\mathbf{B}_0|$ and the dotted line indicates the value of the field modulus according to the demagnetizing factor for each shape, $\gamma_{\text{shape}} \cdot |\mathbf{B}_0|$. The light orange and white blue regions in (f) indicate negative \mathbf{B} values. Parameters used: sphere of $1 \mu\text{m}$ diameter, cylinder of $1 \mu\text{m}$ diameter and 300 nm thickness, ring of $1 \mu\text{m}$ outer diameter, $0.5 \mu\text{m}$ inner diameter and 300 nm thickness

Demagnetizing effects arise naturally in our modeling. In Fig. 14 we show the magnetic field distribution around a micrometer-sized sphere, cylinder and ring, under a homogeneous magnetic field $\mathbf{B}_0 = B_0 \cdot \mathbf{e}_z$ with $B_0 = 30$ mT. The demagnetizing factors for a perfect diamagnet with such geometries are 1.5, 1.8 and 1.8, respectively⁵¹. Our modeling as shown in Fig. 14 perfectly matches the analytically calculated values when λ_L is close to zero, i.e., for an ideal diamagnet. In the case of the ring, flux quantization is partly responsible for the magnetic field distribution within the ring. As indicated in Fig. 14(f), the light section of the curve represents negative values of \mathbf{B} , which are generated by the supercurrent in the ring to keep $\Phi_{\text{hole}} = 0$.

In case of chip-based superconducting traps, deviation from the spherical particle shape and flux quantization result in larger magnetic field gradients, which lead to higher trap frequencies, as we described in Sec. V.

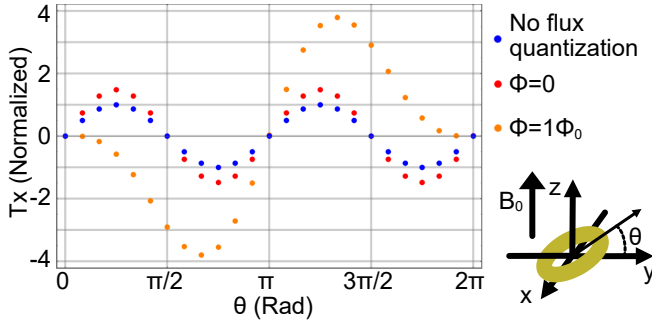


Figure 15. Normalized x component of the torque experienced by a superconducting ring (with inner and outer radii of 0.4 and 0.5 μm , respectively, thickness of 50 nm and $\lambda_L = 50$ nm) with (blue) no flux quantization, (red) with flux quantization and zero trapped flux, and (orange) with one trapped flux quantum parallel to the applied homogeneous field \mathbf{B}_0 . \mathbf{B}_0 has a magnitude such that the flux through the ring equals Φ_0 when $\theta = 0$.

3. Flux quantization: a ring in a homogeneous magnetic field

In general, generating a supercurrent has an energy cost. Then, it follows that the energy of the superconductor is minimized when the amount of supercurrent in it is smallest.

Such an effect is shown in Fig. 15, where we calculate the x component of the torque acting on a superconducting ring in a homogeneous magnetic field \mathbf{B}_0 as a function of the ring's inclination with respect to the y axis. We consider the cases for a superconducting ring with (i) no flux quantization, (ii) flux quantization with zero trapped and (iii) one flux quantum trapped with the same orientation as \mathbf{B}_0 .

The ring with no flux quantization experiences a torque because the field is less perturbed when \mathbf{B}_0 is parallel to

the area of the hole than when it is perpendicular. Hence, it takes less supercurrent to expel the field when $\theta = \pi/2$ or $3\pi/2$. When the area of the hole is perpendicular to \mathbf{B}_0 the torque on the ring vanishes due to symmetry, since it is as likely to tilt clockwise or counter-clockwise, in other words, it is in an unstable equilibrium.

The stable configuration for the ring including flux quantization and no trapped flux, i.e., $\Phi_t = 0$, is to be oriented so that no flux is threading the hole, i.e., $\pi/2$ or $3\pi/2$. The difference is that the torque is stronger due to additional current from flux quantization that keeps $\Phi_t = 0$ when $\theta \neq \pi/2$ or $3\pi/2$.

For the case of a ring with one trapped flux quantum parallel to \mathbf{B}_0 , the configuration in which the least supercurrent is generated is that where \mathbf{B}_0 is parallel to the trapped flux quantum, since \mathbf{B}_0 is chosen so that the flux through the hole equals Φ_0 when the ring is perpendicular to the field. Thus, the ring will experience a torque that will force it to $\theta = 0$. For $\theta = \pi$ the ring will be unstable because the flux through the hole at this configuration is maximum ($\Phi = 2\Phi_0$).

4. Flux quantization: a ring and levitation

Ref.²⁴ provides an analytic formula for the trap frequency along the vertical direction for levitating a ring in a quadrupole field, including flux quantization. We compared FEM-2D simulations to this formula for a ring with inner and outer radii of 0.4 μm and 0.5 μm , respectively, thickness of 50 nm and $\lambda_L = 50$ nm in an AHC trap with coil radius and separation of 10 μm and a current of 3 A. Using FEM-2D and assuming zero flux trapped in the ring, we obtain (212 ± 0.6) kHz, which is in good agreement with the 209 kHz predicted by Ref.²⁴. We also calculated the inductance of a ring with flux quantization with FEM and obtained (2 ± 0.14) pH, which is in good agreement with 1.6 pH predicted by Ref.³⁴.

Appendix C: The effect of meshing

Given that the model is based on FEM, the results are bound to be dependent on the meshing of the system. As mentioned in Appendix A, constructing a mesh fine enough at the surface of the superconducting domains is critical to get reliable results. This dependence is illustrated in Fig. 16, where the trap frequency along z for a 1 μm diameter sphere in an AHC trap (cf. Fig. 3) is calculated via FEM-3D. For these simulations we changed the maximal mesh element size, l_{mesh} , on the surface of the particle resulting in gradually finer meshed particles, see the insets in Fig. 16 and Fig. 17. When reducing l_{mesh} , the FEM meshing algorithm gradually increases the number of mesh elements in the sphere and, thus, reduces the average element area that one mesh element covers. For $l_{\text{mesh}} \lesssim 5 \cdot \lambda_L = 250$ nm, we observe no clear trend of the trap frequency within its uncertainty. How-

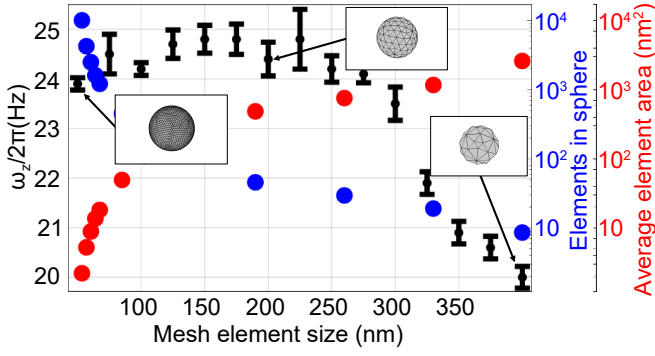


Figure 16. Trap frequency of a spherical particle in an AHC trap as considered in Fig. 3 as a function of the mesh element size l_{mesh} on the particle's surface using FEM-3D. The insets show the mesh on the surface of the particle at the given element sizes.

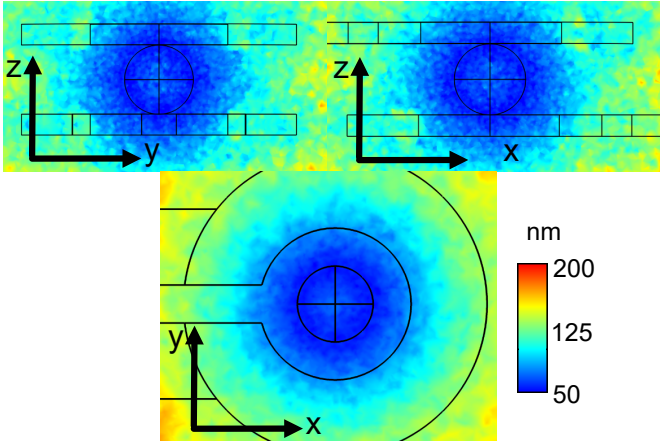


Figure 17. Mesh element size of the FEM-3D model for a superconducting sphere in an AHC-trap, with the maximum element size on the particle surface set to 50 nm. Parameters as in Fig. 3.

ever, for $l_{\text{mesh}} \gtrsim 0.5 \cdot R_{\text{sphere}} = 250$ nm, the particle itself is not properly resolved and the magnetic field penetrates parts or the entire volume of the particle, which effectively increases the effect of field penetration and, thus, decreases the trap frequency.

For FEM-2D we can decrease l_{mesh} further as the computational cost is not as large as for FEM-3D simulations. Fig. 18 shows the trap frequency of a 150 nm radius sphere in an AHC trap in dependence of l_{mesh} . For fine enough meshing, i.e., $l_{\text{mesh}} \lesssim 10$ nm corresponding to $> 10^3$ mesh elements, the FEM simulations converge to the analytical results obtained for a superconducting sphere in a quadrupole field. The small discrepancy is attributed to the difference between the field distribution of a quadrupole field and the real field of the modeled trap.

The trap frequency dependence on the mesh might not only be related to the mesh element size itself, but also on differences in the mesh being differently built for similar

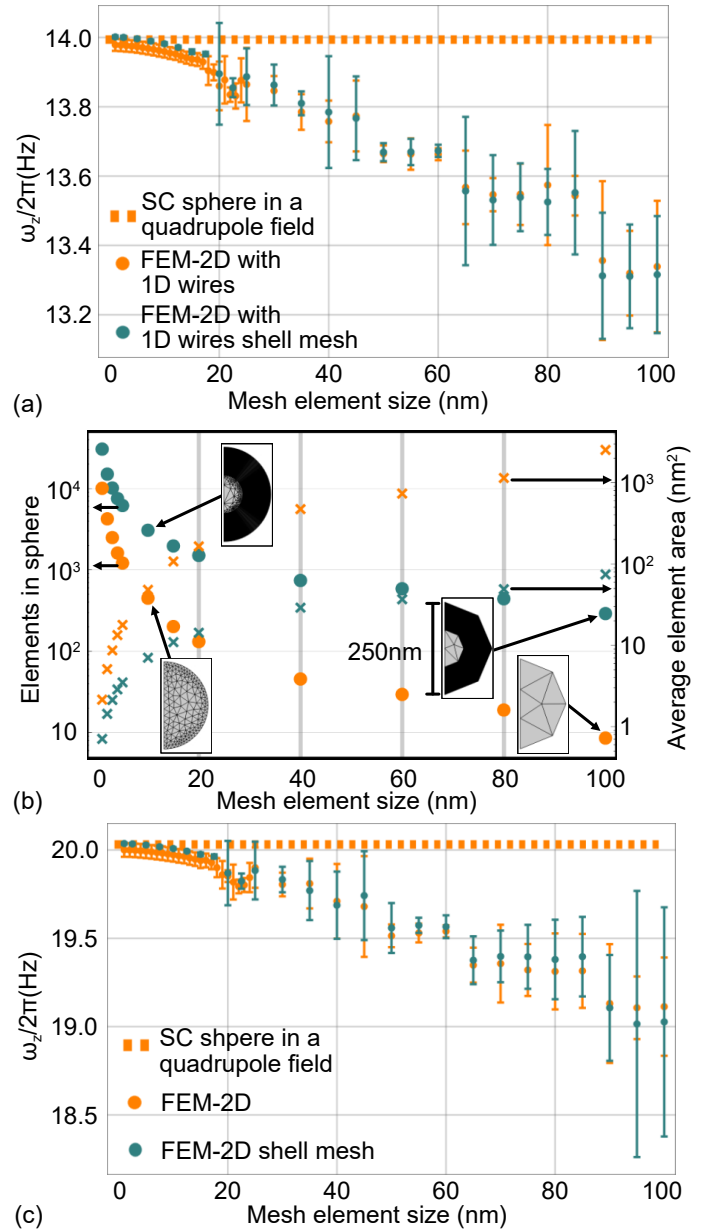


Figure 18. Vertical trap frequency of a spherical particle with 125 nm radius and $\lambda_L = 50$ nm in an AHC trap as considered in Fig. 6 with a scaling factor of 10, as a function of the maximal mesh element size l_{mesh} . Comparison of (a) FEM-2D with 1D-wires and (c) FEM-2D to analytical results obtained for the configuration of a superconducting sphere in a quadrupole field²³ for two different meshing strategies: (i) triangular mesh only (orange data) and (ii) triangular mesh combined with a shell mesh that meshes the outermost volume of 75 nm thickness of the sphere with onion-type layers of 1 nm thickness (green data). (b) Number of mesh elements and average element area for each of the meshing strategies.

FEM models. To test this, we simulated the trap configuration as used for Fig. 16 for slightly different l_{mesh} of (49.9, 49.95, 50.00, 50.05, 50.1) nm and get trap frequencies of (23.7, 23.6, 23.8, 23.6, 23.6) kHz, resulting

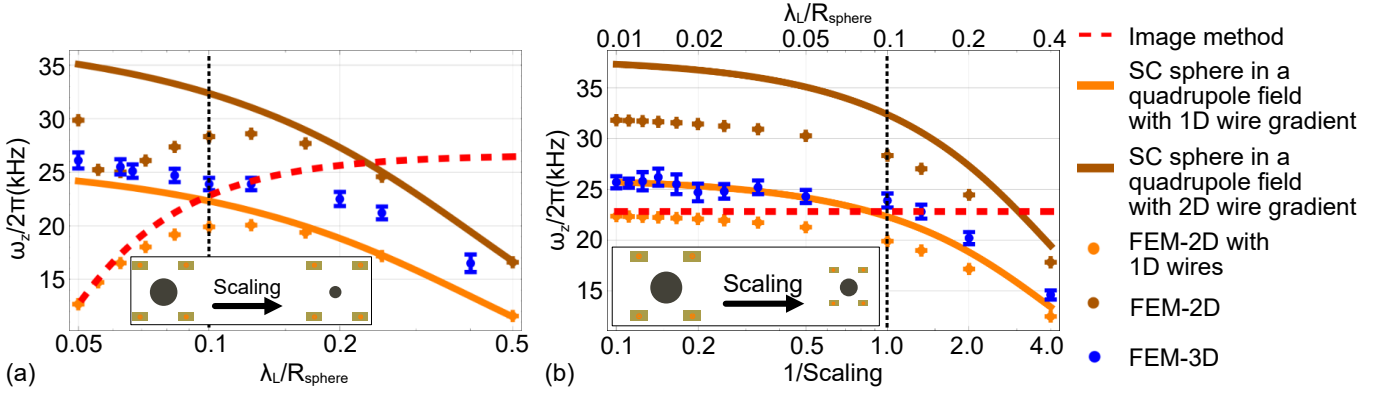


Figure 19. Vertical trap frequency of a superconducting sphere trapped in a realistic AHC predicted by the image method²⁵, by assuming a superconducting sphere in a quadrupole field²³, FEM-2D with 1D-wires, FEM-2D and FEM-3D. (a) The radius of the particle is scaled and the geometrical parameters of the trap and λ_L are kept constant with parameters as given in Tab. I. (b) The geometrical parameters of the trap and particle are taken from Tab. I and scaled by a scaling factor while the current density in the coils and λ_L are kept constant. The vertical dotted black lines indicate the initial geometry. The orange circles in the schematics indicate the location of the current loops in the image method and FEM-2D with 1D-wires calculations.

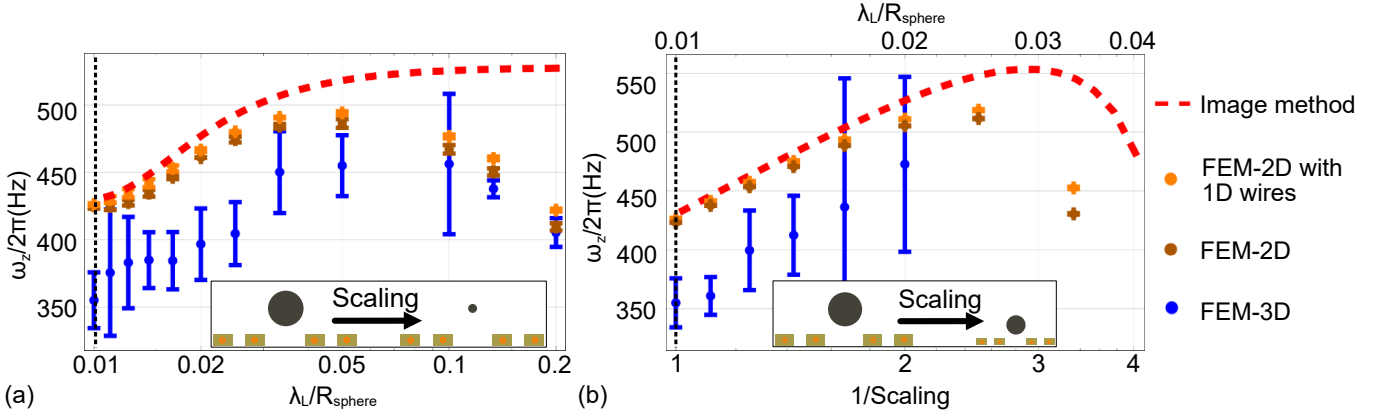


Figure 20. Trap frequency dependence of a superconducting sphere trapped in a realistic double-loop trap. (a) The radius of the particle is scaled and the geometrical parameters of the trap are kept constant (cf. Fig. 8). (b) The geometrical parameters of the trap and the particle are taken from Fig. 8 and scaled by a scaling factor while the current density in the coils and λ_L are kept constant. The vertical black dotted lines indicate the initial geometry. The orange circles in the schematics indicate the location of the current loops in the image method and FEM-2D with 1D-wires calculations.

in a mean value of (23.66 ± 0.09) kHz. Thus, the scatter of trap frequency from using nearly similar meshes of about $\pm 0.4\%$ is smaller than the fit uncertainty for the trap frequency.

Appendix D: Results for centered 1D current loops

Fig. 19 and Fig. 20 show the dependence of the trap frequency for scaling the geometry of the respective trap. Here, we place the 1D current loops in FEM2D with 1D-wires and the image method at the center of the real wires. This data can be compared to the corresponding data shown in Fig. 6 and Fig. 9 when the 1D current loops are placed at the inner corner of the coils.

Appendix E: Magnetic force calculation

In our model, the electromagnetic force and the torque on an object are calculated via the Maxwell stress tensor T , whose components T_{ij} are given as:

$$T_{ij} = \epsilon_0 \left(E_i E_j - \frac{1}{2} \delta_{ij} |\mathbf{E}|^2 \right) + \frac{1}{\mu_0} \left(B_i B_j - \frac{1}{2} \delta_{ij} |\mathbf{B}|^2 \right), \quad (\text{E1})$$

where ϵ_0 and μ_0 are the electrical permittivity and magnetic permeability, respectively, and E_i and B_i are the vector components of the electric and the magnetic field. The knowledge of the field distributions $\mathbf{E}(\mathbf{r})$ and $\mathbf{B}(\mathbf{r})$ is sufficient to calculate electromagnetic forces and torques via surface integrals as⁵²

and

$$\boldsymbol{\tau} = \oint_{\Omega} (\mathbf{r} - \mathbf{r}_0) \times (\mathbf{n}T) dS, \quad (\text{E3})$$

where \mathbf{F} is the force, $\boldsymbol{\tau}$ is the torque, Ω is the surface of the particle and \mathbf{r} and \mathbf{r}_0 are the application point of the force and the center of mass of the particle, respectively.

$$\mathbf{F} = \oint_{\Omega} \mathbf{n}T dS, \quad (\text{E2})$$

-
- ¹ F. Moon and P. Chang, *Superconducting Levitation: Applications to Bearings and Magnetic Transportation* (Wiley, 1994).
- ² E. H. Brandt, *Science* **243**, 349 (1989).
- ³ V. Arkadiev, *Nature* **160**, 330 (1947).
- ⁴ J. M. Goodkind, *Review of Scientific Instruments* **70**, 4131 (1999).
- ⁵ O. Romero-Isart, L. Clemente, C. Navau, A. Sanchez, and J. I. Cirac, *Phys. Rev. Lett.* **109**, 147205 (2012).
- ⁶ M. Cirio, G. K. Brennen, and J. Twamley, *Phys. Rev. Lett.* **109**, 147206 (2012).
- ⁷ M. T. Johnsson, G. K. Brennen, and J. Twamley, *Scientific Reports* **6**, 37495 (2016).
- ⁸ H. Pino, J. Prat-Camps, K. Sinha, B. P. Venkatesh, and O. Romero-Isart, *Quantum Sci. Technol.* **3**, 025001 (2018).
- ⁹ J. Prat-Camps, C. Teo, C. C. Rusconi, W. Wiecezorek, and O. Romero-Isart, *Phys. Rev. Applied* **8**, 034002 (2017).
- ¹⁰ D. F. Jackson Kimball, A. O. Sushkov, and D. Budker, *Phys. Rev. Lett.* **116**, 190801 (2016).
- ¹¹ B. R. Slezak, C. W. Lewandowski, J.-F. Hsu, and B. D’Urso, *New J. Phys.* **20**, 063028 (2018).
- ¹² T. Wang, S. Lourette, S. R. O’Kelley, M. Kayci, Y. Band, D. F. J. Kimball, A. O. Sushkov, and D. Budker, *Phys. Rev. Applied* **11**, 044041 (2019).
- ¹³ C. Timberlake, G. Gasbarri, A. Vinante, A. Setter, and H. Ulbricht, *Appl. Phys. Lett.* **115**, 224101 (2019).
- ¹⁴ A. Vinante, P. Falferi, G. Gasbarri, A. Setter, C. Timberlake, and H. Ulbricht, (2019), arXiv: 1912.12252, arXiv:1912.12252 [quant-ph].
- ¹⁵ J. Gieseler, A. Kabcenell, E. Rosenfeld, J. D. Schaefer, A. Safira, M. J. A. Schuetz, C. Gonzalez-Ballesteros, C. C. Rusconi, O. Romero-Isart, and M. D. Lukin, (2019), arXiv: 1912.10397, arXiv:1912.10397 [quant-ph].
- ¹⁶ D. Zheng, Y. Leng, X. Kong, R. Li, Z. Wang, X. Luo, J. Zhao, C.-K. Duan, P. Huang, J. Du, M. Carlesso, and A. Bassi, *Phys. Rev. Research* **2**, 013057 (2020).
- ¹⁷ M. D. Simon and A. K. Geim, *Journal of Applied Physics* **87**, 6200 (2000).
- ¹⁸ N. Kim, K. Hansen, J. Toppari, T. Suppula, and J. Pekola, *Journal of Vacuum Science & Technology B: Microelectronics and Nanometer Structures Processing, Measurement, and Phenomena* **20**, 386 (2002).
- ¹⁹ T. Nirrengarten, A. Qarry, C. Roux, A. Emmert, G. Nogues, M. Brune, J.-M. Raimond, and S. Haroche, *Phys. Rev. Lett.* **97**, 200405 (2006).
- ²⁰ J. Fortágh and C. Zimmermann, *Rev. Mod. Phys.* **79**, 235 (2007).
- ²¹ V. Dikovskiy, V. Sokolovskiy, B. Zhang, C. Henkel, and R. Folman, *The European Physical Journal D* **51**, 247 (2009).
- ²² S. Bernon, H. Hattermann, D. Bothner, M. Knufinke, P. Weiss, F. Jessen, D. Cano, M. Kemmler, R. Kleiner, D. Koelle, and J. Fortágh, *Nature Communications* **4**, 2380 (2013).
- ²³ J. Hofer and M. Aspelmeyer, *Phys. Scr.* **94**, 125508 (2019).
- ²⁴ C. Navau and A. Sanchez, private communication (2020).
- ²⁵ Q.-G. Lin, *Phys. Rev. B* **74**, 024510 (2006).
- ²⁶ C. Cordier, S. Flament, and C. Dubuc, *IEEE Transactions on Applied Superconductivity* **9**, 2 (1999).
- ²⁷ C. Cordier, S. Flament, and C. Dubuc, *IEEE Transactions on Applied Superconductivity* **9**, 4702 (1999).
- ²⁸ F. Grilli, S. Stavrev, Y. Le Floch, M. Costa-Bouzo, E. Vinot, I. Klutsch, G. Meunier, P. Tixador, and B. Dutoit, *IEEE Transactions on Applied Superconductivity* **15**, 17 (2005).
- ²⁹ A. M. Campbell, *Journal of Superconductivity and Novel Magnetism* **24**, 27 (2011).
- ³⁰ J. C. Simpson, J. E. Lane, C. D. Immer, and R. C. Youngquist, NASA Technical Reports Server (2001).
- ³¹ M. Tinkham, *Introduction to superconductivity*. (Dover publ., 2004).
- ³² D. Niepce, J. J. Burnett, M. G. Latorre, and J. Bylander, *Supercond. Sci. Technol.* **33**, 025013 (2020).
- ³³ C. Navau, N. Del-Valle, and A. Sanchez, *IEEE Transactions on Applied Superconductivity* **23**, 8201023 (2013).
- ³⁴ E. H. Brandt and J. R. Clem, *Phys. Rev. B* **69**, 184509 (2004).
- ³⁵ COMSOL AB, Stockholm, Sweden, “Comsol multiphysics,” www.comsol.com (2019).
- ³⁶ S. Franssila, *Introduction to Microfabrication* (John Wiley & Sons, Incorporated, 2010).
- ³⁷ Y. Asada and H. Nosé, *J. Phys. Soc. Jpn.* **26**, 347 (1969).
- ³⁸ A. Y. Rusanov, M. B. S. Hesselberth, and J. Aarts, *Phys. Rev. B* **70**, 024510 (2004).
- ³⁹ Y. W. Kim, Y. H. Kahng, J.-H. Choi, and S.-G. Lee, *IEEE Transactions on Applied Superconductivity* **19**, 2649 (2009).
- ⁴⁰ A. A. Clerk, M. H. Devoret, S. M. Girvin, F. Marquardt, and R. J. Schoelkopf, *Rev. Mod. Phys.* **82**, 1155 (2010).
- ⁴¹ J. Clarke and A. I. Braginski, *The SQUID Handbook Fundamentals and Technology of SQUIDs and SQUID Systems*, Vol. 1 (Wiley-VCH, Weinheim, 2006).
- ⁴² T. Schurig, *Journal of Physics: Conference Series* **568**, 032015 (2014).
- ⁴³ R. Wölbling, J. Nagel, T. Schwarz, O. Kieler, T. Weimann, J. Kohlmann, A. B. Zorin, M. Kemmler, R. Kleiner, and D. Koelle, *Appl. Phys. Lett.* **102** (2013), 10.1063/1.4804673.
- ⁴⁴ P. Bormann and E. Wielandt, *New Manual of Seismological Observatory Practice 2* (NMSOP2) (2013), 10.2312/GFZ.NMSOP-2.
- ⁴⁵ Y. J. Song, A. F. Otte, V. Shvarts, Z. Zhao, Y. Kuk,

- S. R. Blankenship, A. Band, F. M. Hess, and J. A. Strosio, [Review of Scientific Instruments](#) **81** (2010), [10.1063/1.3520482](#).
- ⁴⁶ M. de Wit, G. Welker, K. Heeck, F. M. Buters, H. J. Eerkens, G. Koning, H. van der Meer, D. Bouwmeester, and T. H. Oosterkamp, [Review of Scientific Instruments](#) **90**, 015112 (2019).
- ⁴⁷ F. Grilli, R. Brambilla, F. Sirois, A. Stenvall, and S. Memiaghe, [Cryogenics](#) **53**, 142 (2013).
- ⁴⁸ A. Morandi, M. D. Ainslie, F. Grilli, and A. Stenvall, [Supercond. Sci. Technol.](#) **30**, 080201 (2017).
- ⁴⁹ F. Grilli, A. Morandi, F. D. Silvestri, and R. Brambilla, [Supercond. Sci. Technol.](#) **31**, 125003 (2018).
- ⁵⁰ J.-G. Caputo, L. Gozzelino, F. Laviano, G. Ghigo, R. Gerbaldo, J. Noudem, Y. Thimont, and P. Bernstein, [Journal of Applied Physics](#) **114**, 233913 (2013).
- ⁵¹ M. Beleggia, D. Vokoun, and M. D. Graef, [Journal of Magnetism and Magnetic Materials](#) **321**, 1306 (2009).
- ⁵² A. Kovetz, *The principles of electromagnetic theory* (CUP Archive, 1990).